Supplementary Information (SI) for Dalton Transactions.
This journal is © The Royal Society of Chemistry 2024

**Electronic Supplementary Information**

# Impact of -OH surface defects on the electronic and structural properties of nickel oxide thin films

Ettore Fois,[a] Chiara Maccato,[b,c] Davide Barreca,*[c] Cristiano Invernizzi,[a] and Gloria Tabacchi*[a]

[a.] *Department of Science and High Technology - Insubria University and INSTM, Via Valleggio 11, 22100 Como, Italy.*

[b.] *Department of Chemical Sciences -Padova University and INSTM, Via Marzolo 1, 35131 Padova, Italy*

[c.] *CNR-ICMATE and INSTM - Department of Chemical Sciences - Padova University, Via Marzolo 1, 35131 Padova, and Corso Stati Uniti 4, 35127 Padova, Italy.*

* Authors to whom correspondence should be addressed; e-mail: davide.barreca@unipd.it ; (D.B.); gloria.tabacchi@uninsubria.it (G.T.).

## Contents

## § S1. Supplementary computational details

### § S1.1 Bulk NiO models

Bulk NiO has a cubic rock-salt structure ($a$ = 4.173 Å)[1] (Fig. S1). The cubic crystallographic unit cell contains four Ni and four O atoms (crystallographic unit cell stoichiometry: $Ni_4O_4$, 8 atoms).
Due to the antiferromagnetic (AF) ordering of NiO, the magnetic unit cell parameter is twice as large as $a$. Hence, the cubic magnetic unit cell corresponds to a 2×2×2 crystallographic unit cell (cubic magnetic unit cell stoichiometry: $Ni_{32}O_{32}$, 64 atoms, Fig. S1a).
It is possible to build a tetragonal 2×2 magnetic unit cell, characterized by AF ordering as well. The tetragonal 2×2 magnetic unit cell stoichiometry is $Ni_{16}O_{16}$, corresponding to 32 atoms (Fig. S1c-d).[2]

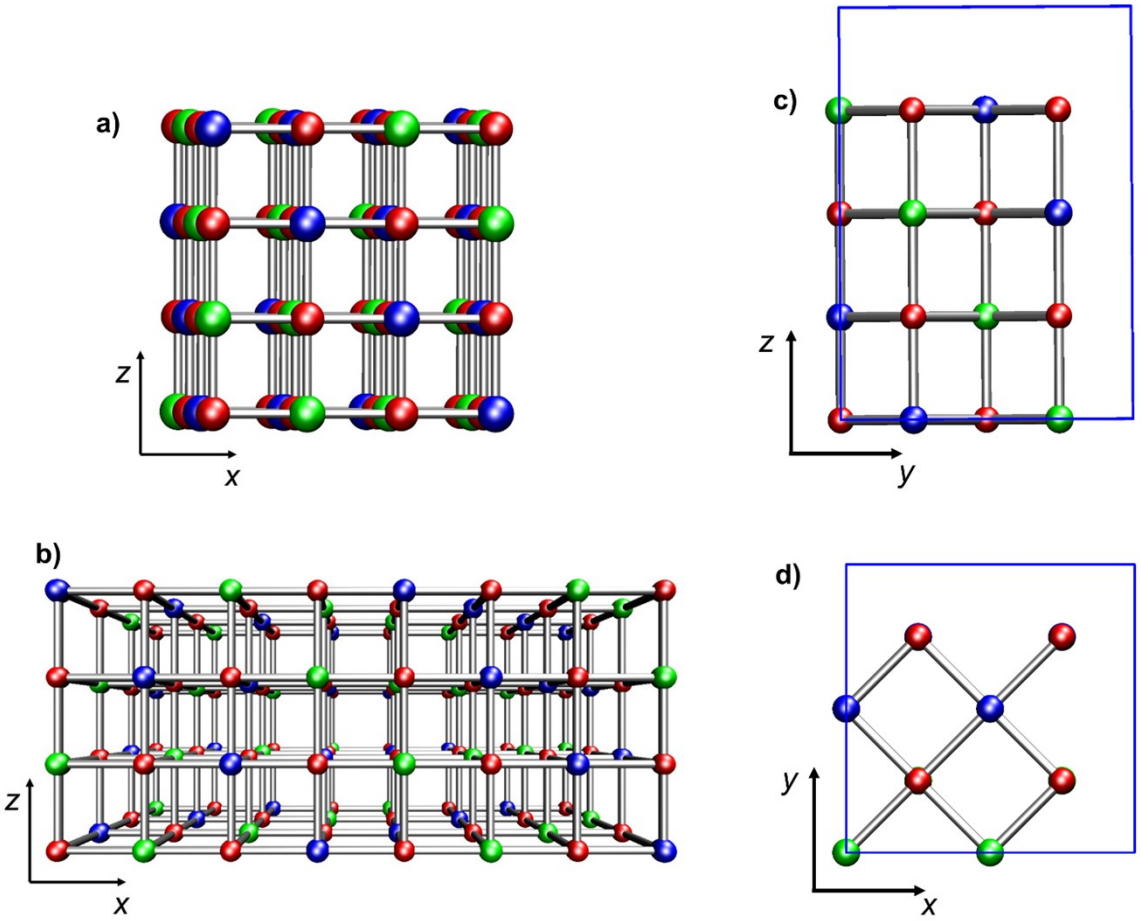


**Fig. S1.** Ball-and-stick representation of the simulation cell of the bulk NiO model systems: **a)** Bulk 1 ($Ni_{32}O_{32}$, cubic 2×2×2 cell) projected on the *xz* plane; **b)** Bulk 2 ($Ni_{64}O_{64}$, orthorhombic 4×2×2 cell) projected on the *xz* plane; **c)-d)** Bulk 3 ($Ni_{16}O_{16}$, tetragonal 2×2 cell) projected on the c) *yz* and d) *xy* planes. Color codes: red, O; blue, Ni (spin-up); green, Ni (spin-down). Blue lines in c)-d) indicate the simulation cell size.

In this work, Density Functional Theory (DFT) calculations on bulk NiO were performed on three different models - denoted Bulk 1, Bulk 2, and Bulk 3 - shown in Fig. S1 and constituted as follows:

1) Bulk 1, containing 64 atoms ($Ni_{32}O_{32}$), and characterized by a cubic simulation cell, corresponding to the cubic 2×2×2 magnetic unit cell (Fig. S1a);

2) Bulk 2, containing 128 atoms ($Ni_{64}O_{64}$), and characterized by an orthorhombic simulation cell, obtained by doubling the cubic magnetic simulation cell along the *x* direction (Fig. S1b);
3) Bulk 3, containing 32 atoms ($Ni_{16}O_{16}$), and characterized by a tetragonal simulation cell, corresponding to the tetragonal 2×2 magnetic unit cell (Fig. S1c-d).

In all bulk models, atomic positions and cell volume were optimized (0 K) at a pressure of 0 Kbar. All atoms were allowed to move during the optimization calculations.

**§ S1.2 Regular NiO(100) slab models**

Two regular (defectless) NiO(100) slabs, shown in Fig. S2, have been built:

1) RegSurf 1, with stoichiometry $Ni_{32}O_{32}$ (64 atoms), derived from Bulk 1, containing four NiO layers and 8 top-layer Ni atoms (4 spin-up, 4 spin-down), surface area: 17.43 $Å^2$;
2) RegSurf 2, with stoichiometry $Ni_{64}O_{64}$ (128 atoms), derived from Bulk 2, containing four NiO layers and 16 top-layer Ni atoms (8 spin-up, 8 spin-down), surface area: 34.86 $Å^2$.

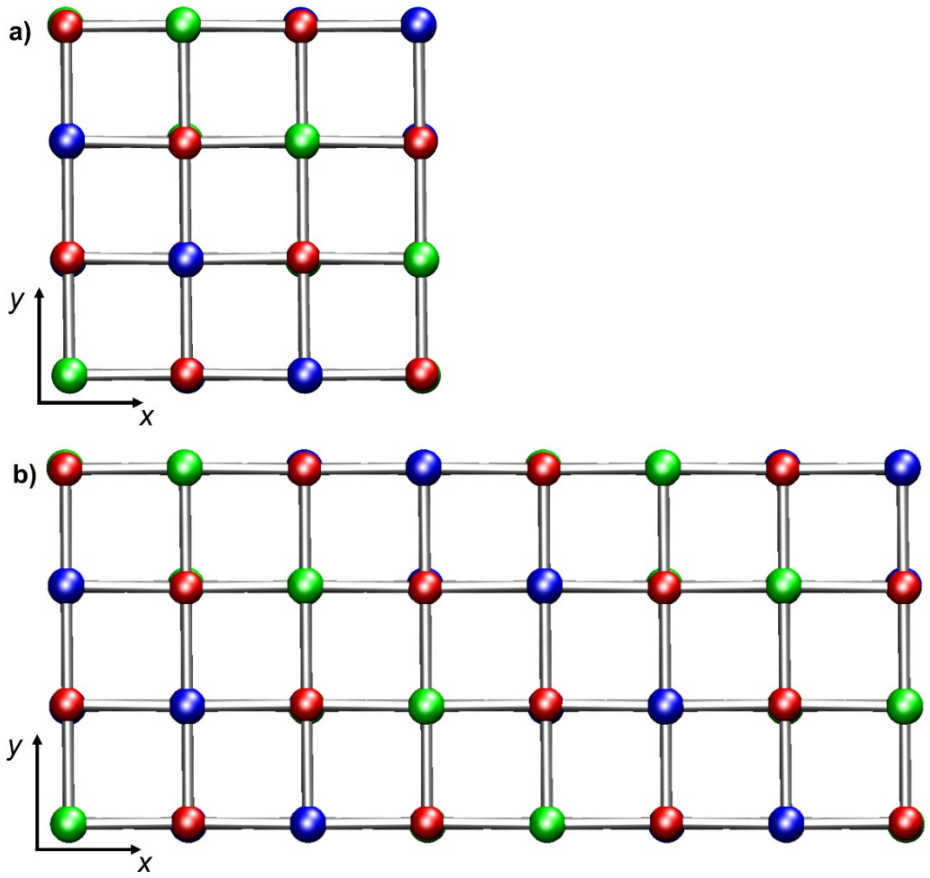


**Fig. S2.** Ball-and-stick representation of the simulation cell of the slab models of the regular NiO(100) surface: **a)** RegSurf 1 ($Ni_{32}O_{32}$) projected on the *xy* plane; **b)** RegSurf 2 ($Ni_{64}O_{64}$) projected on the *xy* plane. Color codes: red, O; blue, Ni (spin-up); green, Ni (spin-down).

A vacuum region of 14 Å along the z direction has been included in the simulation cell of both models. These regular NiO(100) slab models were subjected to optimization of the atomic coordinates, whereas the *a* cell parameter was fixed to the value obtained for the corresponding bulk models. In both cases, the Ni and O atoms in the bottom layer were fixed at their bulk positions.

## § S1.3 Defective NiO(100) slab models

### § S1.3.1 A single –OH group on NiO(100)

As mentioned in the main text, the addition of a –OH group on a Ni atom perturbs unevenly the symmetry of the two magnetic sublattices, affecting thus the system AF ordering . Nonetheless, it is worthwhile investigating how the presence of a single hydroxyl group may affect structural and electronic properties of regular Ni(100) slabs.

In particular, we considered three models, characterized by different simulation cell size, *i.e.* $Ni_{32}O_{32}(OH)$, $Ni_{16}O_{16}(OH)$, and $Ni_{24}O_{24}(OH)$ (see Fig. S3a,b,c, respectively).

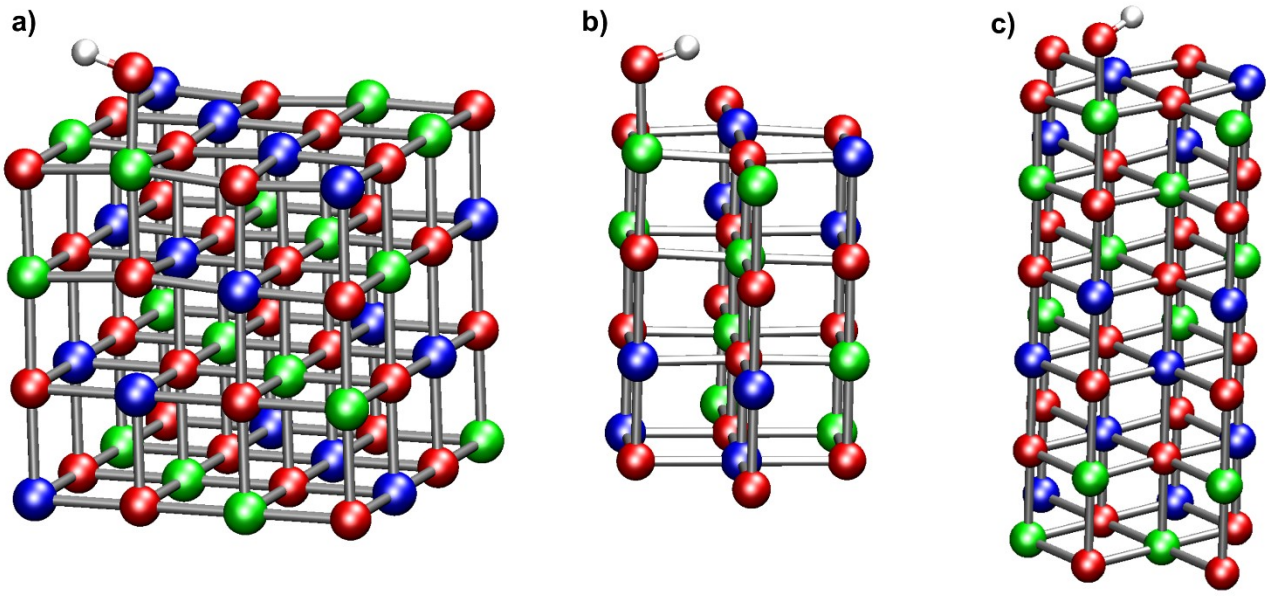


**Fig. S3.** Ball-and-stick representation of the simulation cell of the mono-hydroxylated NiO(100) slab models: **a)** $Ni_{32}O_{32}(OH)$; **b)** $Ni_{16}O_{16}(OH)$; **c)** $Ni_{24}O_{24}(OH)$. Color codes: red, O; blue, Ni (spin-up); green, Ni (spin-down).

The main features of the simulation cells of these three models are summarized as follows:

1) $Ni_{32}O_{32}(OH)$ (66 atoms), containing four NiO layers and 8 top-layer Ni atoms (4 spin-up, 4 spin-down), derived from Bulk 1 (cubic 2×2×2 simulation cell), surface area: 17.43 $Å^2$;
2) $Ni_{16}O_{16}(OH)$ (34 atoms), containing four NiO layers and 4 top-layer Ni atoms (2 spin-up, 2 spin-down), derived from Bulk 3 (tetragonal 2×2 simulation cell), surface area: 8.72 $Å^2$;
3) $Ni_{24}O_{24}(OH)$ (50 atoms), containing six NiO layers and 4 top-layer Ni atoms (2 spin-up, 2 spin-down), derived from Bulk 3 (tetragonal 2×2 simulation cell), surface area: 8.72 $Å^2$.

These mono-hydroxylated NiO(100) slab models were subjected to atomic position optimization. For the four-layer case, the Ni and O atoms in the bottom layer were fixed at their bulk positions, whereas for the six layer model the atom of the two bottom layers were fixed at their bulk coordinates. This choice has been applied even to the other hydroxylated slabs.

A vacuum gap of 14 Å along *z* has been included in the simulation cell of the three models. To assess the convergence of electronic properties with respect to the vacuum gap, calculations on the $Ni_{32}O_{32}(OH)$ model were performed also with a 17 Å vacuum region (see § S4 for results).

### § S1.3.2 Two –OH groups on NiO(100)

The presence of two –OH moieties on Ni(100) was investigated by using models of different surface areas, in order to assess the influence of an increasing concentration of defects.

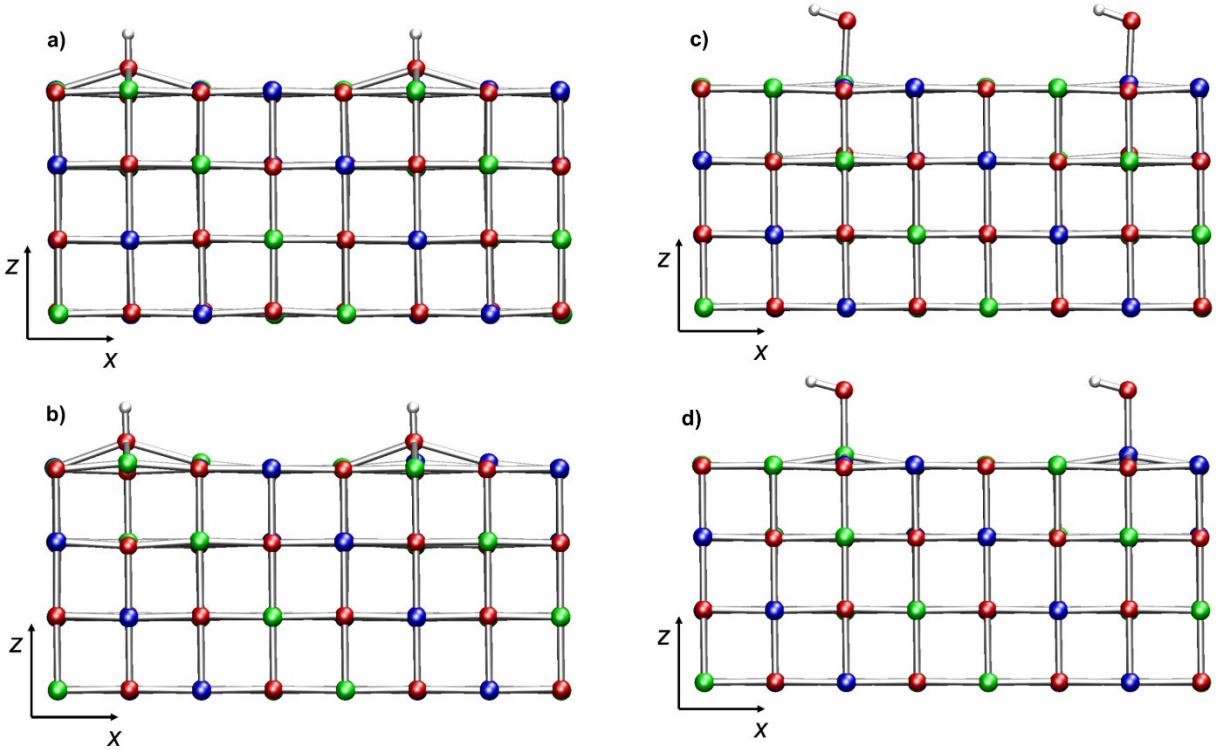


**Fig. S4** Ball-and-stick representation (projected on the *xz* plane) of the optimized structures of di-hydroxylated NiO(100) 4-layer model slabs built from RegSurf 2 and mimicking a low concentration of surface hydroxyl groups: **a)** $(Ni_{64}O_{64})2H+$, containing two $H^+$, each bonded to an O atom of the top layer; **b)** $(Ni_{64}O_{64})2H$, containing two H, each bonded to an O atom of the top layer; **c)**$(Ni_{64}O_{64})2(OH)$, containing two neutral –OH defects; **d)** $(Ni_{64}O_{64})2(OHm)$, containing two negatively charged $–OH^-$ defects. In **c)-d)**, the two -OH groups are bonded to Ni atoms with opposite spin. Color codes: red, O; blue, Ni (spin-up); green, Ni (spin-down), white: H.

To simulate a low concentration of –OH defects, four slab models were built using the largest regular slab, namely RegSurf 2 ($Ni_{64}O_{64}$, surface area: 17.43 $Å^2$) (Fig. S4). Hydroxyl groups on top of Ni(100) can be obtained in two ways, i.e. by adding either an –H atom to an O site, or an –OH group to a Ni site of the Ni(100) top-layer. In addition, the –H (or –OH) ad-atoms may be present also in their charged form (+1 for –H, -1 for –OH). Actually, although the modeling of charged ad-atoms requires particular attention, with regard to the inclusion of a suitable charge background and the use of a sufficiently large supercell, we considered even this situation because it was the only way to simulate charged defects, whose presence on NiO(100) has been documented in the literature by experimental studies.[3]

The first two models (Fig. S4a,b) have the same simulation cell stoichiometry $[Ni_{64}O_{64}]2H$, but they are characterized by different total charges. The first one, bearing two OH groups ($[Ni_{64}O_{64}]2H+$), was obtained by adding two protons to two top layer oxygen atoms and was characterized by total charge +2*e* (Fig. S4a). In this case, a uniform -2*e* negative background was included in the calculations in order to maintain the system electrical neutrality. The second one (electrically

neutral), simulating the presence of two OH groups, was obtained by adding two H atoms to two top layer O atoms (Fig. S4b). In both cases the two H (or H+) were positioned on top of the same top layer oxygens separated by 9.168 Å, the maximum separation compatible with the periodic boundary conditions, see Fig. S4a,b.

The third and fourth models (Fig. S4c,d) have simulation cell stoichiometry $[Ni_{64}O_{64}]2(OH)$.

The third model, denoted as $[Ni_{64}O_{64}]2(OH)$, is electrically neutral, and simulates the adsorption of two OH radicals (Fig. S4c).

In the fourth model, the OH groups were introduced in the anionic OH- form. The negative -2*e* charge was compensated by a +2*e* uniform charge background. This model is referred to as $[Ni_{64}O_{64}]2(OHm)$ (Fig. S4d).

Both $[Ni_{64}O_{64}]2(OH)$ and $[Ni_{64}O_{64}]2(OHm)$ models were obtained by positioning two -OH groups on two top-layer Ni atoms belonging to different magnetic sub-lattices, separated by 9.157 Å, the maximum separation compatible with the periodic boundary conditions, see Fig. S4c,d).

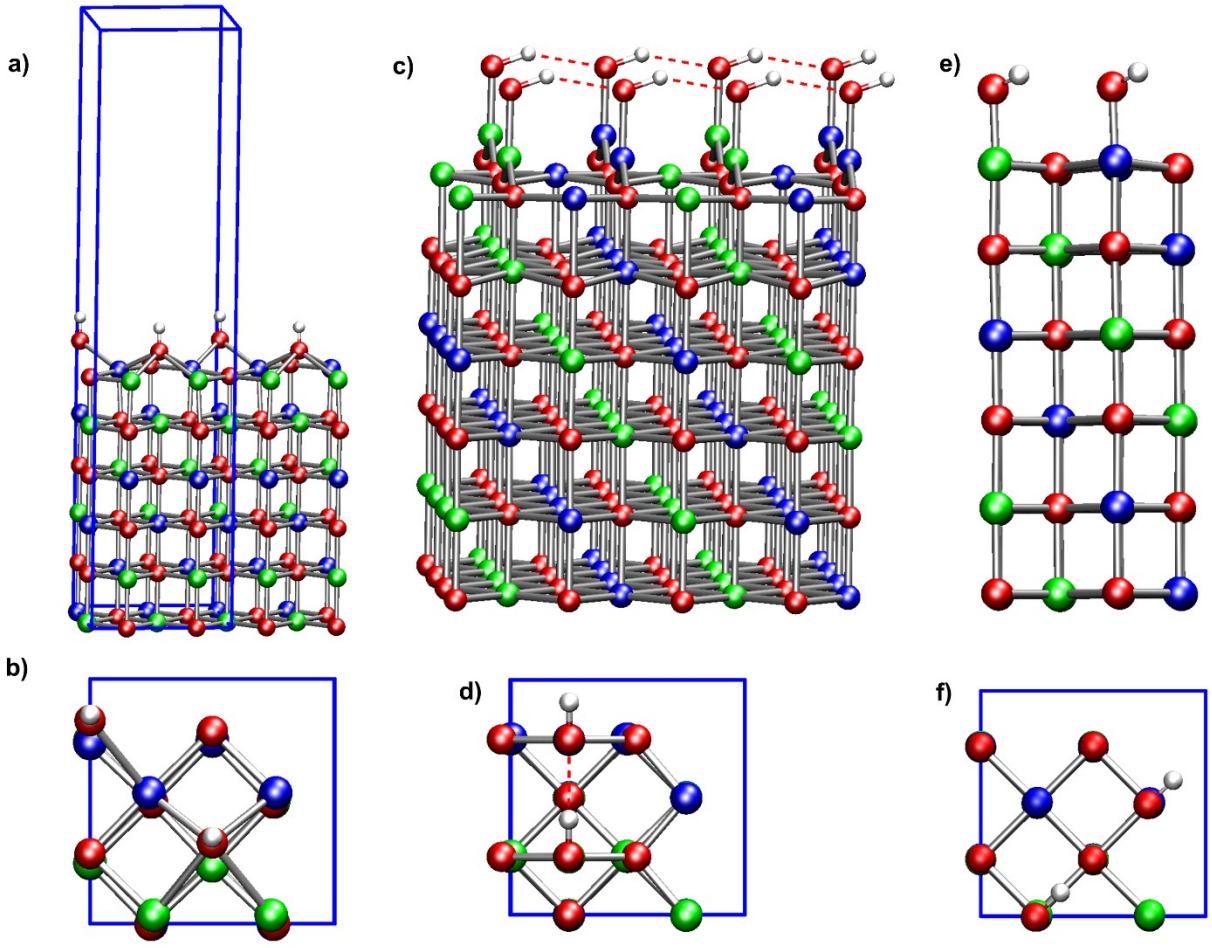


**Fig. S5** Graphical representations of the optimized structures of di-hydroxylated NiO(100) model slabs (6-layer) built with the 2×2 tetragonal cell and mimicking a higher concentration of surface hydroxyl groups. a) side view and b) top view of $(Ni_{24}O_{24})2H$, two containing two H, each bonded to an O atom of the top layer; c) side view and d) top view of $(Ni_{24}O_{24})2(OH)^a$, with two –OH separated by 2.951 Å; e) side view and f) top view of $(Ni_{24}O_{24})2(OH)^b$, with two –OH groups separated by 4.171 Å. The two -OH groups are bonded to Ni atoms with opposite spin. Color codes: red, O; blue, Ni (spin-up); green, Ni (spin-down), white: H; red dashed lines: hydrogen bonds. Blue solid lines indicate the size of the simulation cell.

To simulate a high concentration of –OH defects, three new slab models constituted by 6 NiO layers were built using the tetragonal 2×2 cell, which is characterized by the smallest surface area (8.72 $Å^2$) and exhibits only four Ni centers (Fig. S5). In this case, -H and –OH ad-atoms were included only in their neutral form, *i.e.* no charged defects were considered, due to the small surface area of the 2×2 tetragonal cell.

The first model of this series, denoted $(Ni_{24}O_{24})2H$, was built by adding two –H atoms to two O sites of the top-layer (separated by 4.173 Å) (Fig. S5a,b).

Two models with stoichiometry $(Ni_{24}O_{24})2(OH)$ were built by adding two –OH groups on two Ni-sites of opposite spin, in different locations. In the former case (Fig. S5c,d), the two Ni centers were separated by 2.951 Å, while in the latter (Fig. S5e,f) the distance among the Ni sites was 4.170 Å.

To summarize, we simulated seven models featuring two surface –OH moieties:

1) $Ni_{64}O_{64}2H$ (130 atoms), containing four NiO layers and 16 top-layer Ni atoms (8 spin-up, 8 spin-down), built by adding two –H atoms to two –O sites of RegSurf 2 (charge 0);
2) $[Ni_{64}O_{64}]2H+$ (130 atoms), containing four NiO layers and 16 top-layer Ni atoms (8 spin-up, 8 spin-down), built by adding two –H+ to two –O sites of RegSurf 2 (charge +2);
3) $[Ni_{64}O_{64}]2(OH)$ (132 atoms), containing four NiO layers and 16 top-layer Ni atoms (8 spin-up, 8 spin-down), built by adding two –OH groups to two –Ni sites of RegSurf 2 (charge 0);
4) $[Ni_{64}O_{64}]2(OHm)$ (132 atoms), containing four NiO layers and 16 top-layer Ni atoms (8 spin-up, 8 spin-down), built by adding two –OH- to two –Ni sites of RegSurf 2 (charge -2);
5) $[Ni_{24}O_{24}]2H$ (50 atoms), containing six NiO layers and 4 top-layer Ni atoms (2 spin-up, 2 spin-down), built by adding two –H atoms to two –O of the 2×2 cell top-layer (charge 0);
6) $[Ni_{24}O_{24}]2(OH)^a$ (52 atoms), containing six NiO layers and 4 top-layer Ni atoms (2 spin-up, 2 spin-down), built by adding two –OH groups to two close Ni sites of the 2×2 cell top-layer (charge 0);
7) $[Ni_{24}O_{24}]2(OH)^b$ (52 atoms), containing six NiO layers and 4 top-layer Ni atoms (2 spin-up, 2 spin-down), built by adding two –OH groups to two distant Ni sites of the 2×2 cell top-layer (charge 0).

These di-hydroxylated NiO(100) slab models were subjected to optimization of the atomic coordinates. In cases 1) to 4), we have optimized the *a* cell parameter as well because some of these models bear charged species. The optimized *a* cell parameter resulted 4.100 Å, 4.084 Å, 4.092 Å and 3.980 Å for models 1),2),3),4), respectively.

A vacuum gap of 14 Å along *z* has been included in the simulation cell of all models.

**§ S1.3.3 Four –OH groups on NiO(100)**

The first model, simulating a relatively low concentration of –OH defects, was built by positioning 2 H on two top-layer O atoms and 2 -OH groups on two Ni atoms of opposite spins on RegSurf 2 (the regular slab with the largest surface area). This model (optimized *a* cell parameter: 4.112 Å) mimics a (100) slab with two dissociated water molecules (at low concentration), and it was referred to as $[Ni_{64}O_{64}]2H\text{-}2(OH)$ (Fig. S6a).

By adopting the tetragonal 2×2 cell, we built three models characterized by a lower surface area, and mimicking a high concentration of –OH defects.

The first model of this series, $[Ni_{24}O_{24}]4H$, was built by adding an –H atom on the top of each of the four O sites of the top-layer (Fig. S6b).
The second model, $[Ni_{24}O_{24}]4(OH)$, was built by adding an –OH group on the top of each of the four Ni sites of the top-layer (Fig. S6c).
The third model, denoted as $[Ni_{24}O_{24}]2H\text{-}2(OH)$, was built by adding two –OH groups on two Ni sites of opposite spin (Ni-Ni distance = 4.171 Å), and two –H atoms on the respective neighboring oxygens. This model mimics a NiO(100) slab with two adsorbed dissociated water molecules (at high concentration) (Fig. S6d).

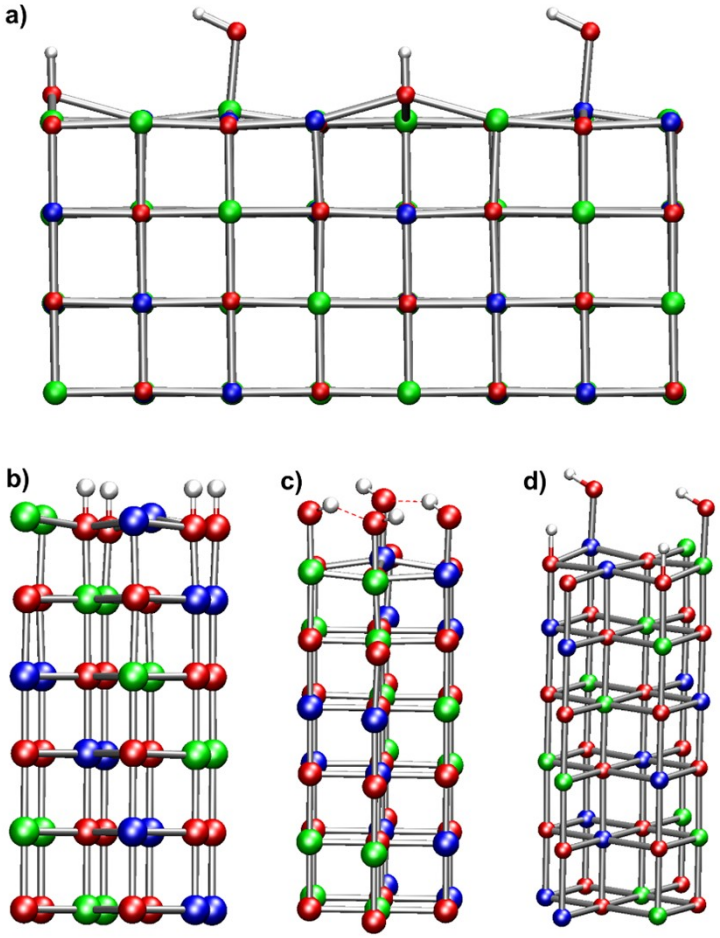


**Fig. S6** Graphical representations (side view) of tetra-hydroxylated NiO(100) slabs: a) $[Ni_{64}O_{64}]2H\text{-}2(OH)$ (optimized structure); b) $[Ni_{24}O_{24}]4H$ (starting configuration); c) $[Ni_{24}O_{24}]4(OH)$ (optimized structure); $[Ni_{24}O_{24}]2H\text{-}2(OH)$ (starting configuration). Color codes: red, O; blue, Ni (spin-up); green, Ni (spin-down), white: H; red dashed lines: hydrogen bonds.

To summarize, we simulated 4 models bearing four surface –OH moieties:

1) $[Ni_{64}O_{64}]2H\text{-}2(OH)$ (134 atoms), containing four NiO layers and 16 top-layer Ni atoms (8 spin-up, 8 spin-down), built by adding two –H atoms to two –O sites and two –OH groups on two Ni sites of RegSurf 2;
2) $[Ni_{24}O_{24}]4H$ (52 atoms), containing six NiO layers and 4 top-layer Ni atoms (2 spin-up, 2 spin-down), built by adding four –H atoms to the four O sites of the 2×2 cell top layer;
3) $[Ni_{24}O_{24}]4(OH)$ (56 atoms), containing six NiO layers and 4 top-layer Ni atoms (2 spin-up, 2

spin-down), built by adding four –OH groups to the four Ni sites of the 2×2 cell top layer;

4) $[Ni_{24}O_{24}]$2H-2(OH) (54 atoms), containing six NiO layers and 4 top-layer Ni atoms (2 spin-up, 2 spin-down), built by adding two –H atoms to two –O sites and two –OH groups on two Ni sites of opposite spin of the 2×2 cell top layer.

These defective NiO(100) slab models were subjected to optimization of the atomic coordinates. A vacuum gap of 14 Å along *z* has been included in the simulation cell of all models.

**§ S1.4 Details on the electronic structure calculations**

In all the structural optimization calculations reported in this study, the spin polarized PBE approximation to DFT[4] in conjunction with D3-bj[5] empirical correction to dispersion interactions was adopted.

In a different way, the electronic structure calculations for obtaining the values of the electronic band gap were performed, on the optimized structures, in the framework of the Hubbard Hamiltonian approach. Indeed, it is well known that Gradient Corrected DFT approximations (GGA) severely underestimate band gaps in transition metal oxides. A simple and viable strategy to overcome this limitation rests on the DFT + U, method, in which the DFT total energy is augmented by a local Hubbard correction, specified by the on-site Coulomb interaction U. Specifically, in all the calculations presented herein, we adopted the simplest version of the Hubbard Hamiltonian methods – namely, a Hubbard U term has been added to the Hamiltonian.[6,7] The selected value of the U term -6.4 eV – is in line with literature data.[8]

The interactions of the valence electrons with the cores were dealt with by employing ultra-soft pseudopotentials[9,10] of the Vanderbilt type for Ni, O and H atoms. In the case of Ni, a semicore pseudopotential was adopted – *i.e.*, only the 1s and 2s-2p shells were included in the core. The 3s, 3p, 3d, and 4s electrons were pseudized.

Concerning the number of valence electrons, the core charge of Ni was 18, hence the 3s, 3p, 3d, and 4s electrons of Ni are explicitly accounted for in the calculations (18 valence electrons for each Ni). The core charge of O was 6, thus the 2s and 2p O electrons are explicitly represented (pseudized) in the calculations (6 valence electrons for each O). Concerning H, its core charge was 1, thus the electron in the 1s state was pseudized (1 valence electron for each H).

In all the calculations reported herein, the electronic states were expanded in planewaves with a cutoff of 60 Ry for the wavefunction (320 Ry for the electron density).

Regarding the bulk models, whereas a 2×2×2 mesh was adopted for the Brillouin zone (BZ) sampling for Bulk 1, a 1×2×2 mesh was adopted for Bulk 2, and a 6×6×4 mesh was employed for Bulk 3.

Concerning the regular Ni(100) slabs, a 2×2×1 mesh was employed for RegSurf 1, while a 1×2×1 mesh was used for RegSurf2.

Calculations on the monohydroxylated Ni(100) slab models were performed by employing 2×2×1, 6×6×1, and 6×6×1 BZ sampling meshes for $Ni_{32}O_{32}$(OH), $Ni_{16}O_{16}$(OH), and $Ni_{24}O_{24}$(OH), respectively.

In the case of di-hydroxylated Ni(100) models, for all the large slabs, built starting from RegSurf 2, a 1×2×1 BZ sampling was adopted, while for all the other slabs a 6×6×1 mesh was employed.

A 6×6×1 mesh was also used for all the tetra-hydroxylated Ni(100) models, with the exception of $Ni_{64}O_{64}$2H2(OH) (1×2×1 mesh, as for RegSurf 2).

## § S2. Supplementary data on bulk models

The structural optimization of the three bulk models (Bulk 1-3) provided identical cell parameter ($a$ = 4.175Å) and interatomic Ni-O and Ni-Ni nearest-neighbor distances (Table 1). A close similarity of the electronic properties of the three models is evidenced by the energy band gap ($E_{gap}$) values in Table 1, and by the density of states (DOS), shown in Fig. S7.

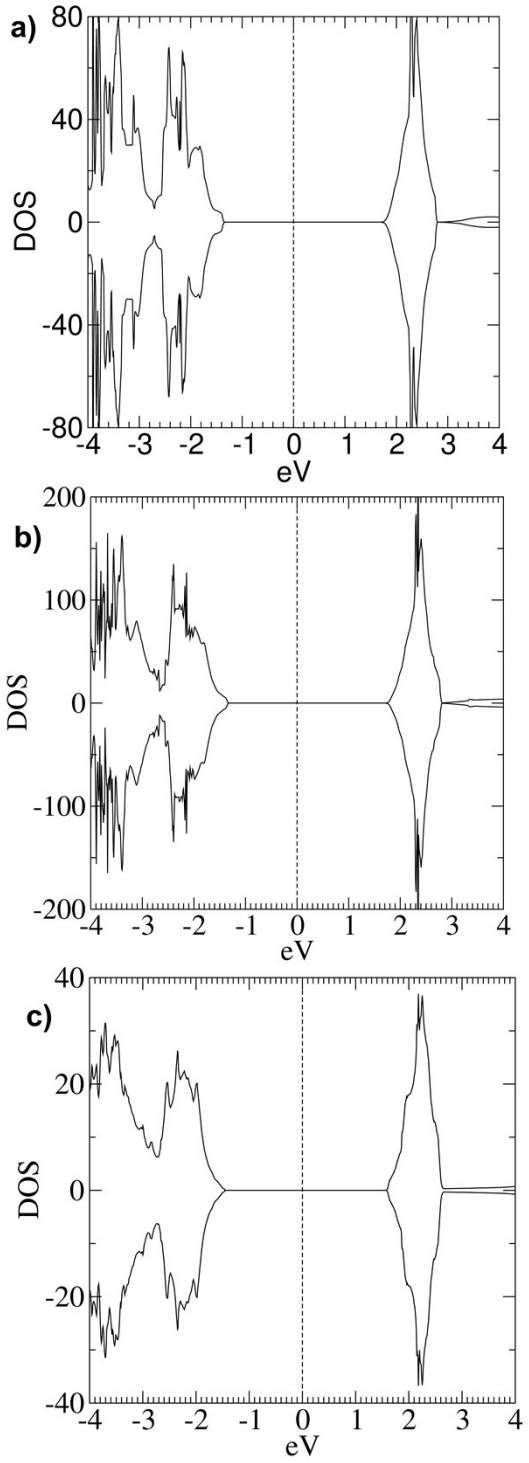


**Fig. S7** DOS computed for bulk model systems: a) Bulk 1, $Ni_{32}O_{32}$; b) Bulk 2, $Ni_{64}O_{64}$; c) Bulk 3, $Ni_{16}O_{16}$. The vertical dashed line represents the Fermi level position. Positive and negative curves represent spin-up and spin-down components, respectively.

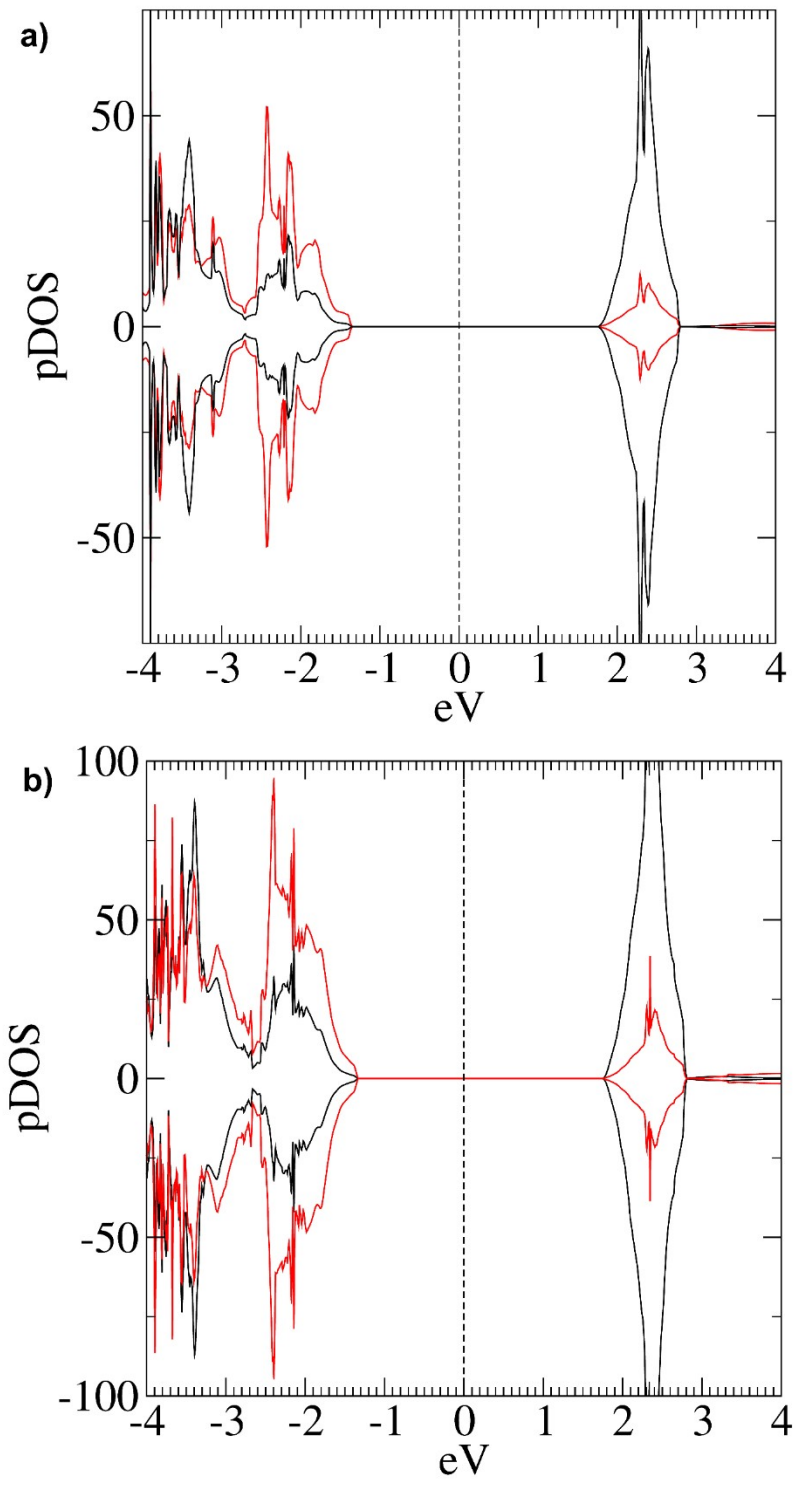


**Fig. S8** pDOS computed for bulk model systems: a) $Ni_{32}O_{32}$; b) $Ni_{64}O_{64}$. The black vertical dashed line represents the Fermi level position. Positive curves: spin-up components; negative curves: spin down components; red lines: oxygen states; black lines: Ni *d*-states.

The partial DOS (pDOS) calculated for Bulk 1 and Bulk 2 are compared in Fig. S8. As can be seen, the two systems have very similar pDOS. In both cases, the pDOS indicates a higher density of oxygen 2p states at the top of the valence band (VB), and a higher density of empty Ni *d*-states at the bottom of the conduction band (CB).

## § S3. Supplementary data on regular NiO(100) surfaces

The pDOS computed for RegSurf 1 and RegSurf 2 are compared in Fig. S9. As already noticed for the corresponding bulk systems (see Fig. S8), the two slab models are characterized by analogous pDOS. In both cases, as found for the bulk models, the pDOS features a higher density of oxygen 2p states at the top of the VB (with a minor contribution of the Ni-*d* states), and a higher density of empty Ni *d*-states at the bottom of the CB.

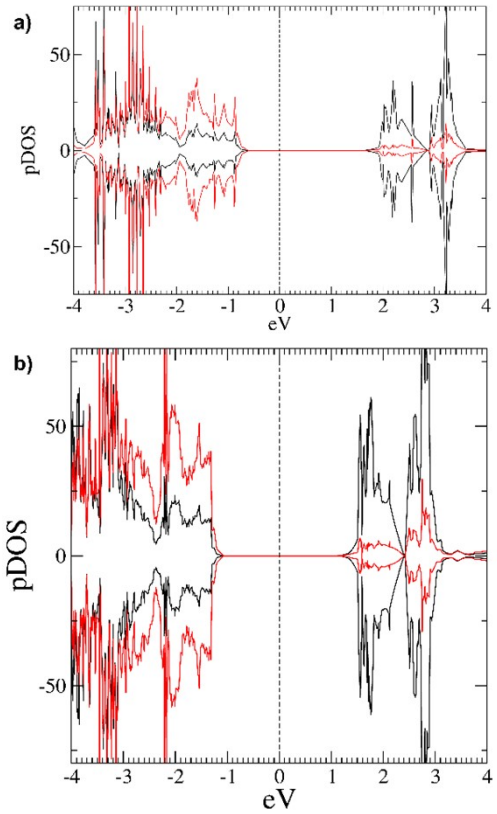


**Fig. S9** pDOS computed for regular slab model systems: a) $Ni_{32}O_{32}$; b) $Ni_{64}O_{64}$. The black vertical dashed line represents the Fermi level position. Positive curves: spin-up components; Negative curves: spin down components; red lines: oxygen states; black lines: Ni *d*-states.

The structural features of RegSurf 1 and RegSurf 2 are very similar. In both slab models, the surface relaxation affects mostly the top layer (see Table 1, main text). In the second layer, the difference between short and long Ni-O distances is less pronounced*, i.e.*, 2.082 Å and 2.091 Å, respectively, in the case of $Ni_{32}O_{32}$. Additionally, atoms in the second layer are all closer to the third layer, being 2.070 Å the average interlayer separation. This behaviour of the Ni-O distances in NiO (100) topmost layers, which affects evenly the two magnetic sub-lattices, is in line with the results of scanning tunnelling microscopy (STM) experiments on NiO surfaces.[11]

## § S4. Results on mono-hydroxylated NiO(100) models

The minimum energy structures computed for $Ni_{32}O_{32}(OH)$, $Ni_{16}O_{16}(OH)$, and $Ni_{24}O_{24}(OH)$ are represented in Fig. S3a,b,c, respectively, while relevant properties are reported in Table S1 (atom

labels in Fig. S10). In discussing the structural properties of these slabs, we will mainly focus on the O*-Ni*-OH atoms (Fig. S10) *i.e.*, on the local features of the defect.

As can be seen from the data reported in Table S1, the structural properties of the three slabs are very similar. In all cases, identical O-H bond lengths are obtained. Importantly, the –OH moiety forms a strong bond with a top-layer Ni center, denoted as Ni* (Fig. S10). The formation of the Ni*-OH bond leads to a significant increase of the Ni*-O* distance with respect to the bulk value (2.086 Å), suggesting a weakening of the Ni*-O* bond. This effect is more pronounced for the slabs characterized by a smaller surface area, *i.e.* $Ni_{16}O_{16}$(OH) and $Ni_{24}O_{24}$(OH).

**Table S1.** Properties of mono-hydroxylated slab models. $E_{gap}$: band gap energy; $\mu_{tot}$: total magnetization; $\mu_{Ni}$: absolute magnetization per Ni atom. Energies in eV, $\mu_{tot}$ and $\mu_N$ in Bohr Magnetons ($\mu_B$), Ni*-OH, O-H, Ni-O and Ni*-O*distances in Å, Ni*-$\hat{O}$-H angles in degrees.

| System | $E_{gap}$ | Type | $\mu_{tot}$ | $\mu_{Ni}$ | Ni*-OH | O-H | <Ni-O>[c] | Ni*-O* | Ni*-$\hat{O}$-H |
|---|---|---|---|---|---|---|---|---|---|
| **$Ni_{32}O_{32}$(OH)[a]** | 0 | *Half-metal* | -0.91 | 1.81 | 1.817 | 0.980 | 2.081 | 2.118 | 107.2 |
| **$Ni_{32}O_{32}$(OH)[b]** | 0 | *Half-metal* | -0.91 | 1.81 | 1.817 | 0.980 | 2.081 | 2.118 | 107.2 |
| **$Ni_{16}O_{16}$(OH)[a]** | 0 | *Half-metal* | -1.00 | 1.81 | 1.808 | 0.980 | 2.100 | 2.148 | 107.7 |
| **$Ni_{24}O_{24}$(OH)[a]** | 0 | *Half-metal* | -1.00 | 1.77 | 1.808 | 0.980 | 2.100 | 2.152 | 107.2 |

[a] Computed with a vacuum gap of 14 Å. [b] Computed with a vacuum gap of 17 Å. [c] Average Ni-O distance for the top-layer.

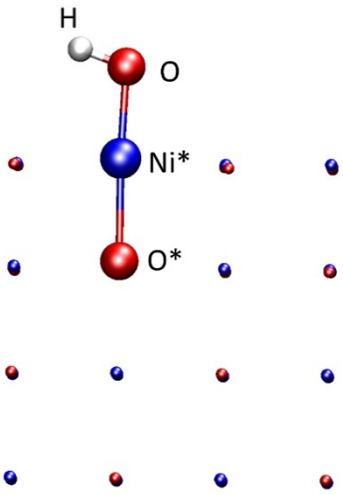


**Fig. S10** Ball-and-stick representation of the local environment of the –OH defect (depicted as larger spheres) with pertaining atom labels in monohydroxylated model slabs. Ni* is the top-layer Ni center bearing the –OH group, O* is the lower-layer oxygen atom bonded to Ni*. Color codes: red, O; blue, Ni, white: H.

In addition, the values of the Ni*-$\hat{O}$-H bond angle are very similar among the considered models (Table S1). Beside the close similarity in the local –OH environment, the three slabs are also characterized by very similar values of the average Ni-O bond distance <Ni-O> between top-layer Ni and O atoms (Table S1).

Overall, this analysis indicates that the thickness of the slab barely affects the structure of the hydroxylated slabs. In a different way, the surface area appears to have an appreciable effect – namely, the deviations of the Ni-O distances from the bulk value (2.086 Å) are emphasized in the smaller-surface $Ni_{16}O_{16}$(OH) and $Ni_{24}O_{24}$(OH) models, characterized by 4 top-layer Ni atoms.

As mentioned in the main text, the addition of a single –OH group on a Ni atom unevenly perturbs the two magnetic sublattices, which are no longer symmetric between each other. This symmetry

breaking affects the magnetic and electronic properties of the systems. Indeed, all the models are characterized by a total magnetization $\mu_{tot}$ different from zero (Table S1). Such an effect is slightly more pronounced in the models with a smaller surface area. More importantly, the electronic structure is significantly altered, with the appearance of a half-metallic character (Table S1), as also evidenced by the DOS shown in Fig. S11.

The convergence of structural, electronic, and magnetic properties of the largest model ($Ni_{32}O_{32}(OH)$) with respect to the size of the vacuum gap has been verified by performing calculations using two supercells characterized by 14 Å and 17 Å vacuum, respectively. The data in Table S1 and the DOS in Fig. S11a clearly indicate that convergence *vs*. vacuum gap size is reached with a 14 Å gap.

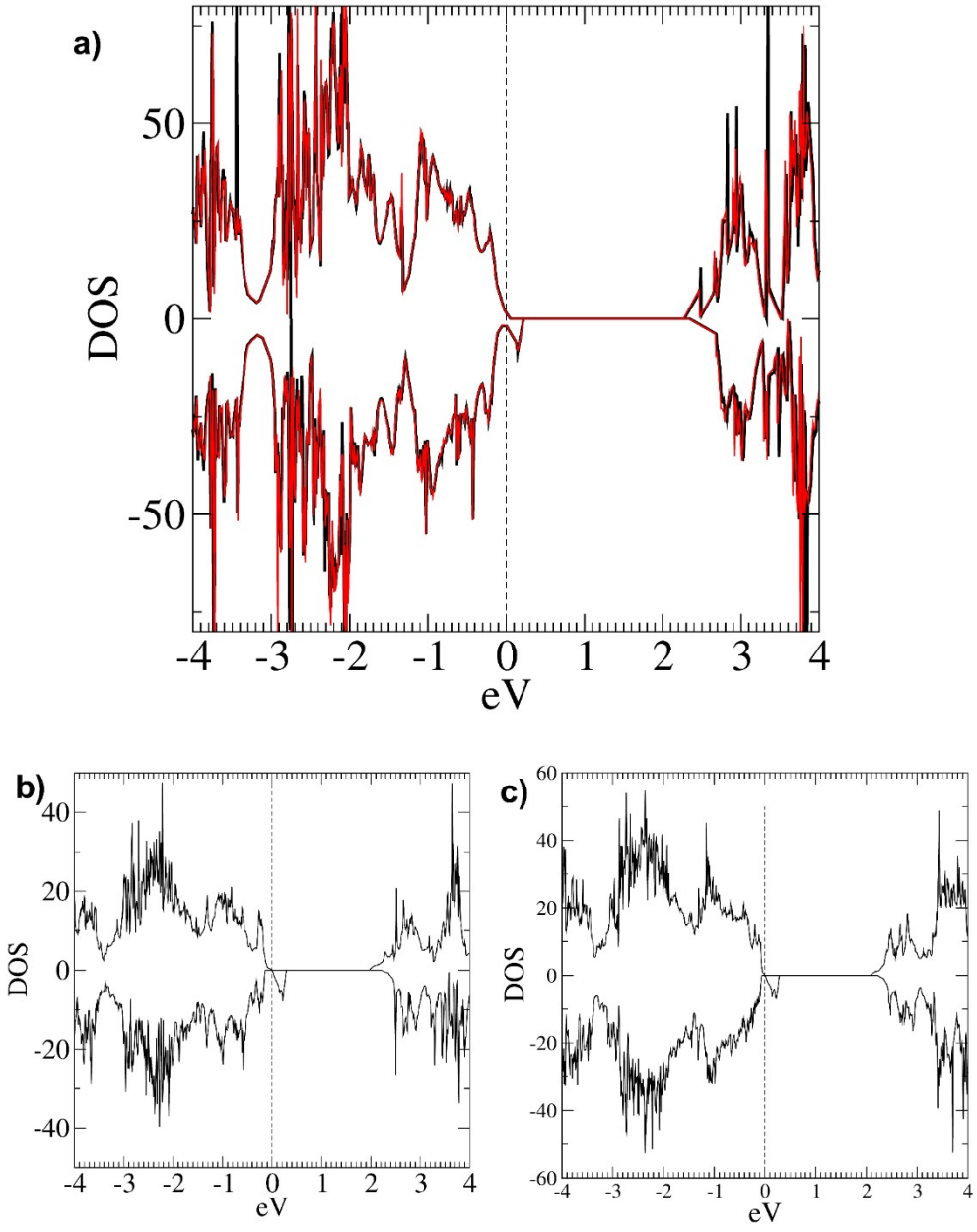


**Fig. S11** DOS computed for mono-hydroxylated slab model systems: **a)** $Ni_{32}O_{32}(OH)$; **b)** $Ni_{16}O_{16}(OH)$; **c)** $Ni_{24}O_{24}(OH)$. The black vertical dashed line represents the Fermi level position. Positive curves: spin-up components; negative curves: spin down components. The black and red curves in **a)** are calculated using simulation cells with a vacuum gap of 14 Å and 17 Å, respectively.

## § S5. Supplementary Results on di-hydroxylated NiO(100) models

### § S5.1 Lower –OH concentration

Besides the models discussed in the main text, *i.e*. $Ni_{64}O_{64}$(2H) and $Ni_{64}O_{64}$2(OH), we considered two models bearing charged $H^+$ and $OH^-$ defects (denoted as [$Ni_{64}O_{64}$]2H+ and $Ni_{64}O_{64}$2(OHm), respectively) in order to have some insight about the effect of a low concentration of charged species on the structural, electronic, and magnetic properties of NiO(100) surfaces.
In this Section, further details on the optimized geometry of the neutral slab systems $Ni_{64}O_{64}$(2H) and $Ni_{64}O_{64}$2(OH) are reported, along with a thorough discussion on the structural and electronic properties of the charged models [$Ni_{64}O_{64}$]2H+ and $Ni_{64}O_{64}$2(OHm).

#### § S5.1.1 [$Ni_{64}O_{64}$]2H structural properties

In the optimized structure of [$Ni_{64}O_{64}$]2H (Fig. S4b) the separation between OH groups, is 9.168 Å, whereas the OH bond length is 0.978 Å. The distance of the OH oxygen from the nearest Ni in the layer below (denoted as Ni*, see Scheme 1a, main text) is 2.905 Å, indicating that these O atoms are ≈ 0.7 Å outward from the top layer. The top layer corrugation is more pronounced with respect to the regular slab, with Ni top-layer atoms always upward with respect to O ones (with the exception of the H-bearing oxygens).

#### § S5.1.2 [$Ni_{64}O_{64}$]2(OH) structural properties

The minimum energy structure of this model (Fig. S4c) is characterized by an OH-OH separation of 9.157 Å. In the Ni*-O-H groups (see Scheme 1b, main text), the OH bond length is 0.979 Å, the Ni*-O one is 1.825 Å and the Ni*-O-H bond angle is 106.7°. The OH-bearing Ni* atoms are at 2.032 Å from the nearest oxygen atoms of the layer below (O*, see Scheme 1b, main text), which are slightly shifted upward with respect to the other layer atoms (Fig. S4c). Even in this case, the top layer is corrugated, with Ni atoms positioned slightly upward (≈0.1 Å) with respect to oxygen atoms. Moreover, the system exhibits bond distances between top layer- and second layer atoms ranging from 2.008 Å to 2.117 Å.

#### § S5.1.3 [$Ni_{64}O_{64}$]2H+

The minimum energy structure for this model is shown in Fig. S4a. The optimized cell parameter (4.084 Å) is slightly smaller than the corresponding bulk value (4.175 Å). Basically, the structural properties of this charged slab are very similar to those pertaining to the neutral [$Ni_{64}O_{64}$]2H model**.** The top layers present a slightly corrugated morphology, as found also for the non-defective slabs, with the *z* component of Ni atoms higher by 0.05 Å than the *z* component of O atoms. In contrast, the two oxygen atoms bearing the two protons are significantly displaced outward with respect to Ni atoms. Both Ni*-O-H groups (Scheme 1a, main text) are characterized by a Ni*-O bond distance of 2.806 Å, the O-H bond is 0.982 Å and the Ni*-O-H angle is 179.5°. The two protons are separated by 9.130 Å.

Interestingly, the Ni-O distance in Ni-OH groups is significantly larger than the average Ni-O

separation between top- and second-layer atoms (2.077 Å). This value is smaller than the Ni-O distance between second- and third-layer atoms (2.107 Å). Even in this model, an alternation of short and long Ni-O bond lengths is detected in the Ni-O bond distances between atoms in the top layer. Nevertheless, such an alternating bond pattern is less regular than that found in the stoichiometric slabs, due to the presence of the two OH groups in the top layer (see Fig. S4a).

The band gap for this *p*-type system (1.790 eV) is further decreased with respect to both the bulk and the regular slabs, but no intra-gap states are detected (see Table S2). The pDOS for this model slab (Fig. S12a) indicates an electronic structure analogous to both the bulk and regular surface models. It worth observing that the Fermi level calculated for the $[Ni_{64}O_{64}]2H+$ system is very close to the top of the VB. The AF ordering is maintained and $\mu_{Ni}$ is 1.82 $\mu_B$ as in the regular slab (Table S2).

**Table S2.** Electronic and magnetic properties of the charged di-hydroxylated slabs. $E_{gap}$: band gap energy; $E_{VB}$: top VB energy; $E_{CB}$: bottom CB energy; $E_{intra\text{-}gap}$: energy of intra-gap states; $\mu_{tot}$: total magnetization; $\mu_{Ni}$: absolute magnetization per Ni atom. Energies are in eV, $\mu_{tot}$ and $\mu_N$ in Bohr Magnetons ($\mu_B$), distances in Å. For slab models, distances refer to top-layer atoms. $E_{VB}$ and $E_{CB}$ values are relative to the Fermi Energy, conventionally set to 0.

| system | $E_{gap}$ | $E_{VB}$ | $E_{CB}$ | $E_{intra\text{-}gap}$ | Type | $\mu_{tot}$ | $\mu_{Ni}$ |
|---|---|---|---|---|---|---|---|
| $(Ni_{64}O_{64})2(H^+)$ | 1.790 | -1.270 | 0.520 | - | *p* | 0 | 1.82 |
| $(Ni_{64}O_{64})2(OHm)$ | 1.149 (1.29) | -0.165 | 1.129 | -0.02 | *p* | 0 | 1.82 |

### § S5.1.4 $[Ni_{64}O_{64}]2(OHm)$

The minimum energy structure for this model is shown in Fig. S4d.The introduction of two negatively charged OH defects causes a decrease of the cell parameter to 3.980 Å. Nonetheless, the geometrical features of $[Ni_{64}O_{64}]2(OHm)$ (Fig. S4d) closely resemble the ones exhibited by the neutral $[Ni_{64}O_{64}]2(OH)$ model (Fig. S4c).

In the negatively charged $[Ni_{64}O_{64}]2(OHm)$ system, the O-H bond distances are both equal to 0.977Å. Each hydroxyl O atom is bonded to a top layer Ni* (NI*-OH distance: 1.895 Å), which, in turn, is separated by 2.385 Å from the nearest second layer oxygen O* (Scheme 1b, main text). The Ni*-O-H bond angle is 105.3°. Hence, the OH-bearing Ni* atoms are shifted upward with respect to the other atoms in the layer. As found in all the previously described slabs, the top layer is corrugated, presenting the Ni atoms shifted upward by ≈0.1 Å with respect to the oxygen atoms. In particular, the corrugation of the top layers in $[Ni_{64}O_{64}]2(OHm)$ is very similar to the $[Ni_{64}O_{64}]2(OH)$ case (see Figs. S4c,d). The AF ordering is maintained, and $\mu_{Ni}$ is 1.82 $\mu_B$. The pDOS (Fig. S12b) highlights the *p*-type character of this system, as well as the appearance of an occupied state in the gap. The main contribution to this state results from the 2*p*-states of the adsorbed O atoms. Moreover, this state is located below the Fermi level, suggesting that it is filled by electrons belonging to the two negatively charged $–OH^–$ groups.

As found for the neutral $[Ni_{64}O_{64}]2(OH)$ slab, there is a higher density of O states at the VB top. In a different way, the density of Ni *d*-states and O states at the bottom of the CB are quite similar, whereas, at higher energies, the Ni-*d*-states become predominant.

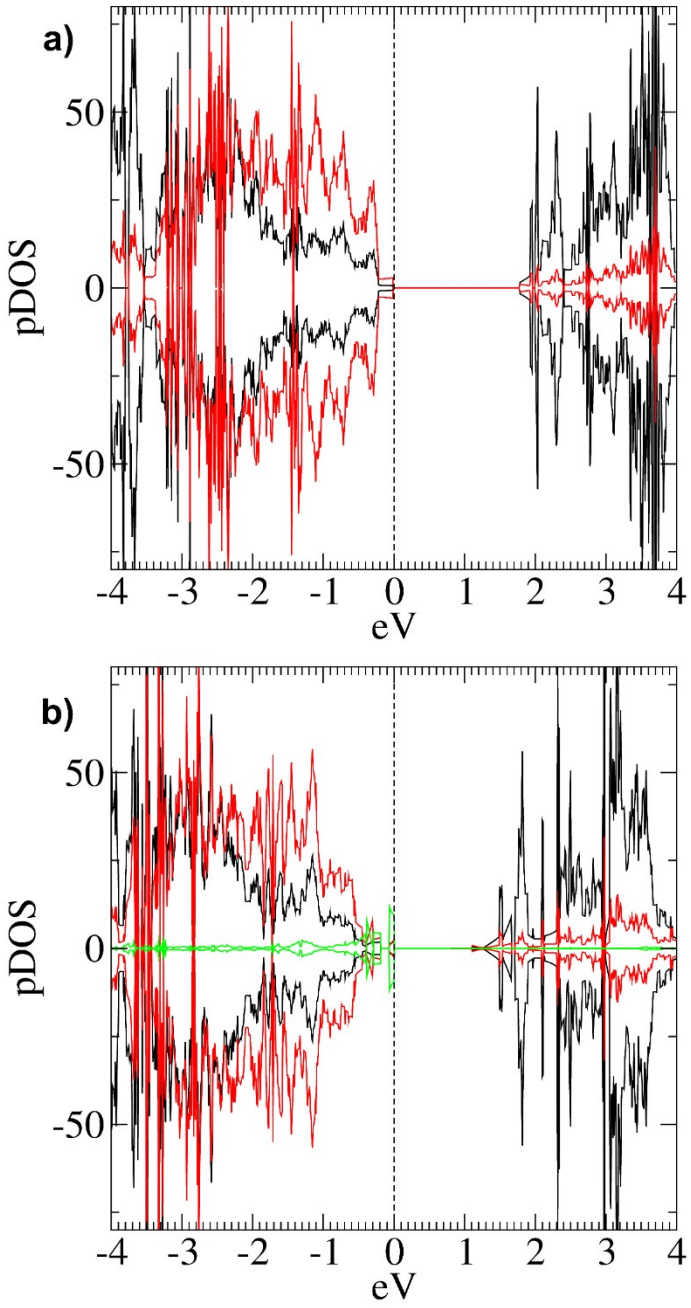


**Fig. S12** pDOS computed for the charged defective slab models: a) $[Ni_{64}O_{64}]2H+$; b) $[Ni_{64}O_{64}]2(OHm)$. The vertical dashed line at 0 eV represents the Fermi level position. Positive curves: spin-up components; negative curves: spin down components; red lines: oxygen states; black lines: Ni *d*-states.

## § S5.2 Higher -OH concentration

### § S5.2.1 $[Ni_{24}O_{24}]2H$

The magnetic and electronic properties of this model are discussed in the main text. The peculiar arrangement of the hydroxyl groups on the system top layer is illustrated in Fig. S13.

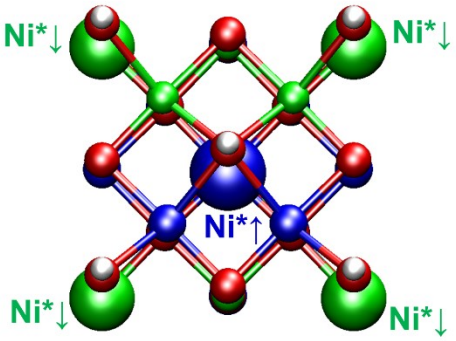


**Fig. S13** Graphical representation of the arrangement of the surface hydroxyl defects in $[Ni_{24}O_{24}]2H$ with respect to the two magnetic spin sublattices. Each OH is on top of a Ni* cation, and it is surrounded by four OH defects on opposite spin Ni* centers.

The –OH bond lengths amount to 0.980 Å. Each –OH is bridging two top-layer Ni* centers of different spin (Fig. S13), with distances of 2.175 Å and 2.454 Å, respectively, whereas the separation of the hydroxyl oxygen from Ni* is 3.037 Å. The corresponding distances in $[Ni_{64}O_{64}]2H$ were 0.980, 2.174 Å, 2.208 Å, and 2.905, respectively. This comparison indicates that structural distortions with respect to regular NiO(100) become more pronounced with increasing defect density.

### § S5.2.2 $[Ni_{24}O_{24}]2(OH)$

The properties of the two models with this stoichiometry, i.e., $[Ni_{24}O_{24}]2(OH)^a$ and $[Ni_{24}O_{24}]2(OH)^b$, exhibiting –OH groups separated by 2.951 and 4.171 Å, respectively, are discussed in the main text. The pDOS for $[Ni_{24}O_{24}]2(OH)^a$ and $[Ni_{24}O_{24}]2(OH)^b$ are shown in Fig. S14a,b, respectively. The two models, in spite of their metallic electronic structures, show different pDOS patterns, since the structures of the top-layers of the two models are significantly different (see Fig. 6 in the main text).

In the $[Ni_{24}O_{24}]2(OH)^a$ case (Fig. S14a), the Fermi Level is positioned in a region where O2p states are predominant, with a minor participation of the Ni-d states. Interestingly, the contribution of the atoms directly linked to the defect (green and blue lines in Fig. S14a) is appreciable in this region. Between the top of the metallic band – located at +0.383 eV from the Fermi Energy - and the bottom of the next empty band there is a 1.91 eV wide region with no electronic states.
This pDOS pattern appears to be closely related to that found for the $[Ni_{64}O_{64}]2(OH)$ model (see Fig. 5b in the main text). Such a system, characterized by a lower surface density of hydroxyl groups, exhibited a very narrow electronic gap (0.250 eV) between the VB top and an empty state located very close to the Fermi Level (+0.021 eV, see Table 2), to which the atoms directly involved in the defect (Ni* and hydroxyl oxygen) contribute significantly. On this basis, it can be reasonably argued that the increase of –OH surface density on passing from $[Ni_{64}O_{64}]2(OH)$ (surface area: 34.86 $Å^2$) to $[Ni_{24}O_{24}]2(OH)^a$ (surface area: 8.72 $Å^2$) has significantly altered the electronic structure of the slab, inducing a transformation from a small-gap p-type semiconductor to a metallic system. In addition, it is worthwhile noting that the distance between two –OH defects is drastically lowered (from 9.157 Å to 2.951 Å) upon passing from $[Ni_{64}O_{64}]2(OH)$ to $[Ni_{24}O_{24}]2(OH)^a$.

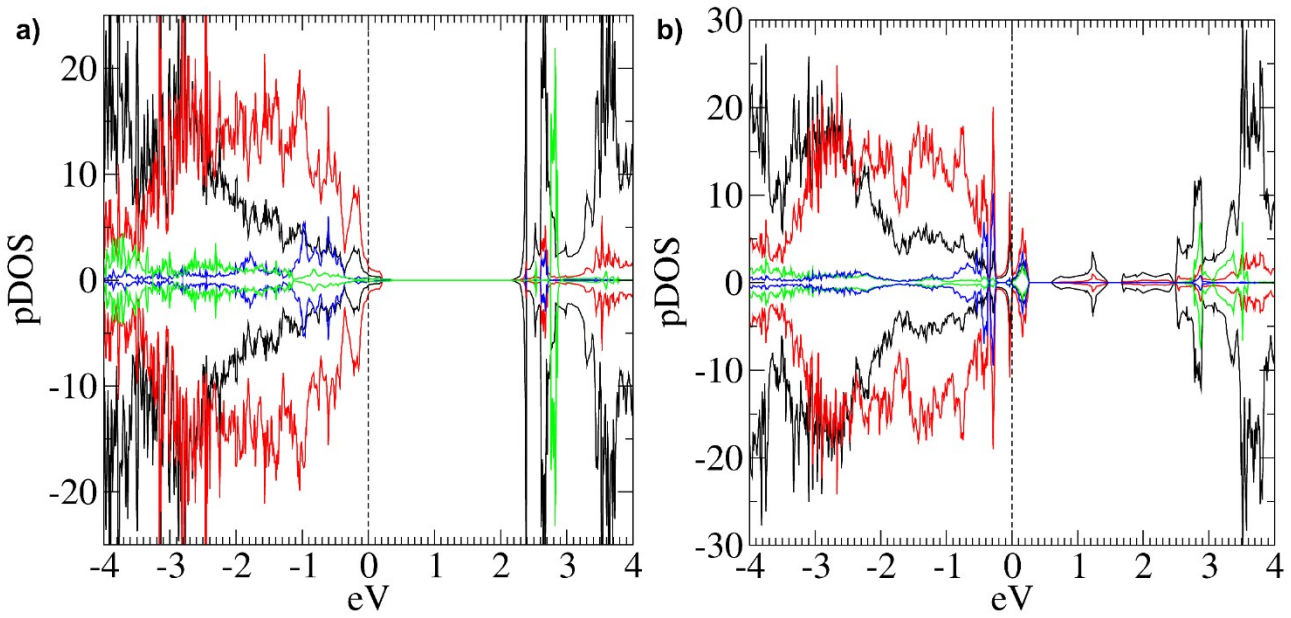


**Fig. S14** pDOS computed for: a) $[Ni_{24}O_{24}]2(OH)^{a;}$ b) $[Ni_{24}O_{24}]2(OH)^{b}$. The vertical dashed line at 0 eV represents the Fermi level position. Positive curves: spin-up components; negative curves: spin down components; black lines: nickel *d*-states; red lines: oxygen states; green lines: d-states of the Ni atoms bearing the –OH groups (Ni*); blue lines: 2p states of the hydroxyl oxygen atoms.

Concerning the $[Ni_{24}O_{24}]2(OH)^{b}$ pDOS (Fig. S14b), the Fermi Level is located in a region characterized by a high density of both O2p states and Ni-d states. The contribution of Ni* d-states and hydroxyl oxygen states at the Fermi Level is lower than that obtained for the $[Ni_{24}O_{24}]2(OH)^{a}$ model (Fig. S14a). Nonetheless, a high density of defect states is clearly distinguishable immediately above the Fermi Level.

In addition, several empty states (with negligible contribution of Ni* and hydroxyl O atoms) are found in the region between the top of the metallic band and the bottom of the next empty band. Such differences with respect to the $[Ni_{24}O_{24}]2(OH)^{b}$ case may be ascribed to the diverse structural features of the top-layer, in particular the larger separation between –OH groups (4.173 Å).

## § S6 Supplementary results on tetra-hydroxylated models

### § S6.1.1 $[Ni_{64}O_{64}]2H$-2(OH)

In this model, shown in Fig. 8 in the main text, the two H atoms are at 0.981 Å from the top layer oxygen to which they are linked, which, in turn, are at 2.781 Å from the nearest Ni of the second layer (Ni*, see Scheme 1a in the main text). The Ni*-O-H angles are 178.4°, and the O-H bonds are nearly perpendicular to the top layer, as found for the $[Ni_{64}O_{64}]2H$ and $[Ni_{64}O_{64}]2H+$ models.

As regards the two OH groups bonded to top layer Ni atoms (Ni*-OH distances = 1.871 Å), the O-H bond lengths are both 0.977 Å. The Ni atoms bearing -OH groups (Ni*, see Scheme 1b in the main text) are at 2.309 Å from the nearest O atoms of the second layer. Even in this model, top layers are corrugated, with Ni atoms typically shifted upward with respect to O ones (except for the H- bearing oxygens). The average separation between top layer and second layer is 2.070 Å, while the separation between second and third layer is 2.094 Å.

### § S6.1.2 $[Ni_{24}O_{24}]4H$

As discussed in the main text, the optimized structure (Fig. S15) is very different from the initial guess (Fig. S6b) due to an important top layer reconstruction. Only two of the four Ni* are at bond distances (2.110 Å) from the O atoms of the second layer (Fig. S15a). These two Ni* cations (of opposite spin) are also bonded to two hydroxyl oxygens each, hence they are three-coordinated. The other two Ni* cations are tetracoordinated by the O atoms of the four –OH groups (Fig. S15b). Such tetracoordinated Ni* are separated by 2.535 Å from the plane of the second layer, and by 2.730 Å from the closest second-layer oxygen. This reconstruction is due to the displacement of the top layer with respect to the second layer by ≈ 0.898 Å in the [-110] direction (see arrow in Fig. S15b).

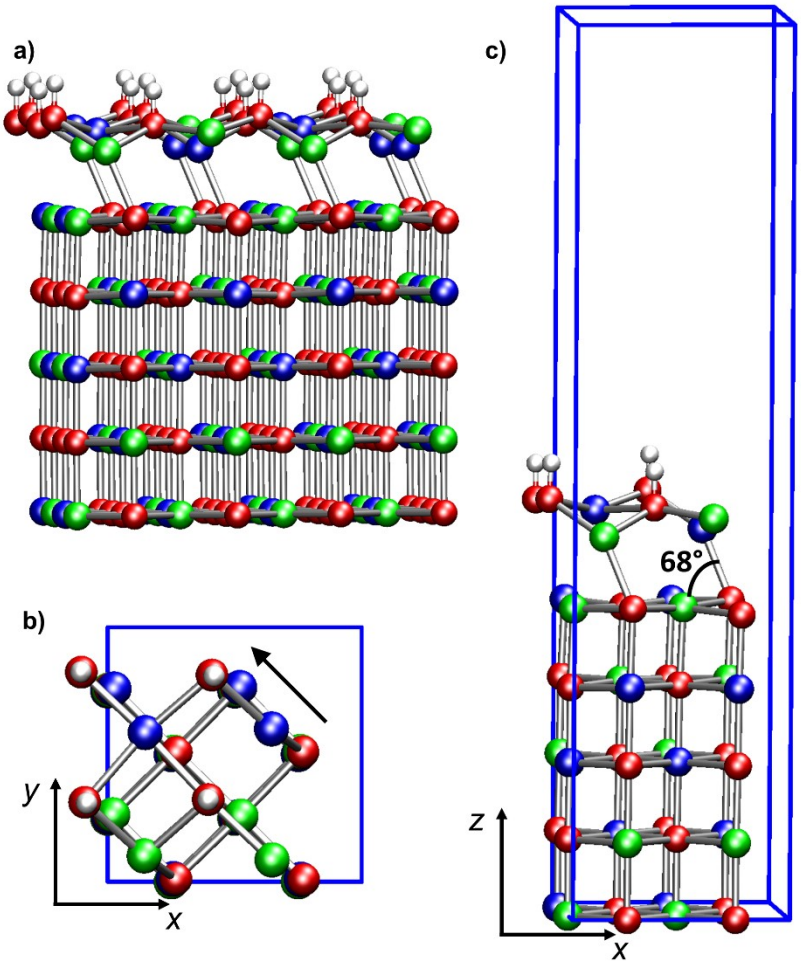


**Fig. S15** Graphical representation of the minimum energy structure of the $[Ni_{24}O_{24}]4H$ system: a) side view; b) simulation cell top view; c) simulation cell side view. Color codes: red: O; blue: spin-up Ni; green: spin-down Ni; white: H. The blue lines indicate the simulation cell.

The Ni-O-Ni angle between the top and the second layer is 68° (Fig. S15c), highlighting the significant deformation with respect to the regular NiO(100) surface, characterized by a Ni-O-Ni angle of 90°. As found for the $[Ni_{64}O_{64}]2H$ and $[Ni_{24}O_{24}]2H$ systems, the O-H bonds are nearly parallel to the *z*-direction. The O-H distances occur in pairs (0.983 Å and 0.980 Å).
The distances of the tetracoordinated Ni* from the hydroxyl oxygens are 2.088 Å, 2.049 Å, 2.183 Å, and 2.140 Å – hence, the Ni* environment is characterized by two short and two long Ni*-O bonds. The four O-Ni-O angles are: 94.8°, 91.4°, 83.5°, and 86.5°.

## § S7. References


1 G. A. Sawatzky and J. W. Allen, *Phys. Rev. Lett.*, 1984, **53**, 2339–2342.

2 A. M. Ferrari, C. Pisani, F. Cinquini, L. Giordano and G. Pacchioni, *J. Chem. Phys.*, 2007, **127**, 174711.

3 J. M. McKay and V. E. Henrich, *Phys. Rev. B*, 1985, **32**, 6764–6772.

4 J. P. Perdew, K. Burke and M. Ernzerhof, *Phys. Rev. Lett.*, 1996, **77**, 3865–3868.

5 S. Grimme, S. Ehrlich and L. Goerigk, *J. Comput. Chem.*, 2011, **32**, 1456–1465.

6 M. Cococcioni and S. De Gironcoli, *Phys. Rev. B*, 2005, **71**, 035105.

7 L. Li and Y. Kanai, *Phys. Rev. B*, 2015, **91**, 235304.

8 M. Nolan, R. Long, N. J. English and D. A. Mooney, *J. Chem. Phys.*, 2011, **134**, 224703.

9 D. Vanderbilt, *Phys. Rev. B*, 1990, **41**, 7892–7895.

10 K. F. Garrity, J. W. Bennett, K. M. Rabe and D. Vanderbilt, *Comput. Mater. Sci.*, 2014, **81**, 446–452.

11 M. R. Castell, S. L. Dudarev, G. A. D. Briggs and A. P. Sutton, *Phys. Rev. B*, 1999, **59**, 7342–7345.